A multiscale study of the mechanisms controlling shear velocity anisotropy in the San Andreas Fault Observatory at Depth

Naomi L. Boness[1] and Mark D. Zoback[2]

ABSTRACT

We present an analysis of shear velocity anisotropy using data in and near the San Andreas Fault Observatory at Depth (SAFOD) to investigate the physical mechanisms controlling velocity anisotropy and the effects of frequency and scale. We analyze data from borehole dipole sonic logs and present the results from a shear-wave-splitting analysis performed on waveforms from microearthquakes recorded on a downhole seismic array. We show how seismic anisotropy is linked either to structures such as sedimentary bedding planes or to the state of stress, depending on the physical properties of the formation. For an arbitrarily oriented wellbore, we model the apparent fast direction that is measured with dipole sonic logs if the shear waves are polarized by arbitrarily dipping transversely isotropic (TI) structural planes (bedding/fractures). Our results indicate that the contemporary state of stress is the dominant mechanism governing shear velocity anisotropy in both highly fractured granitic rocks and well-bedded arkosic sandstones. In contrast, within the finely laminated shales, anisotropy is a result of the structural alignment of clays along the sedimentary bedding planes. By analyzing shear velocity anisotropy at sonic wavelengths over scales of meters and at seismic frequencies over scales of several kilometers, we show that the polarization of the shear waves and the amount of anisotropy recorded are strongly dependent on the frequency and scale of investigation. The shear anisotropy data provide constraints on the orientation of the maximum horizontal compressive stress $S_{H\max}$ and suggest that, at a distance of only 200 m from the San Andreas fault (SAF), $S_{H\max}$ is at an angle of approximately 70° to the strike of the fault. This observation is consistent with the hypothesis that the SAF is a weak fault slipping at low levels of shear stress.

INTRODUCTION

Shear-wave velocity anisotropy is commonly referred to as shear-wave splitting because a shear wave traveling into an anisotropic medium separates into two quasi-shear waves. At a given receiver the fast and slow quasi-shear waves are characterized by their orthogonal polarization directions (Figure 1a) and by a delay between their arrival times. Numerous examples of documented shear-wave anisotropy in the upper crust exist, and various mechanisms have been proposed to explain these observations, including lithologic alignment of minerals/grains (e.g., Sayers, 1994; Johnston and Christensen, 1995; Hornby, 1998); sedimentary bedding planes (e.g., Alford, 1986; Lynn and Thomsen, 1986; Willis et al., 1986); aligned macroscopic fractures (e.g., Mueller, 1991, 1992; Liu et al., 1993; Meadows and Winterstein, 1994); extensive dilatancy anisotropy of microcracks (e.g., Crampin and Lovell, 1991); and the preferential closure of fractures in rock with a quasi-random distribution of macroscopic fractures resulting from an anisotropic stress field (Boness and Zoback, 2004).

These mechanisms can be divided into two major categories. The first category is stress-induced anisotropy in response to an anisotropic tectonic stress state (Figure 1b). This could arise in a medium in which there are aligned microcracks or the preferential closure of fractures in a randomly fractured crust. In this case, vertically propagating seismic waves are polarized with a fast direction parallel to the open microcracks (Crampin, 1986), or perpendicular to the closed macroscopic fractures (Boness and Zoback, 2004), in both cases parallel to the maximum horizontal compressive stress $S_{H\max}$. The second category is structural anisotropy attributable to the alignment of parallel planar features such as macroscopic fractures, parallel sedimentary bedding planes, or the alignment of minerals/grains (Figure 1c). In this case the vertically propagating shear waves exhibit a fast polarization direction parallel to the strike of the structural fabric. In geophysical exploration, shear velocity anisotropy is commonly modeled with a transversely isotropic (TI) symmetry (Figure 1a), whereby the shear waves are polarized parallel
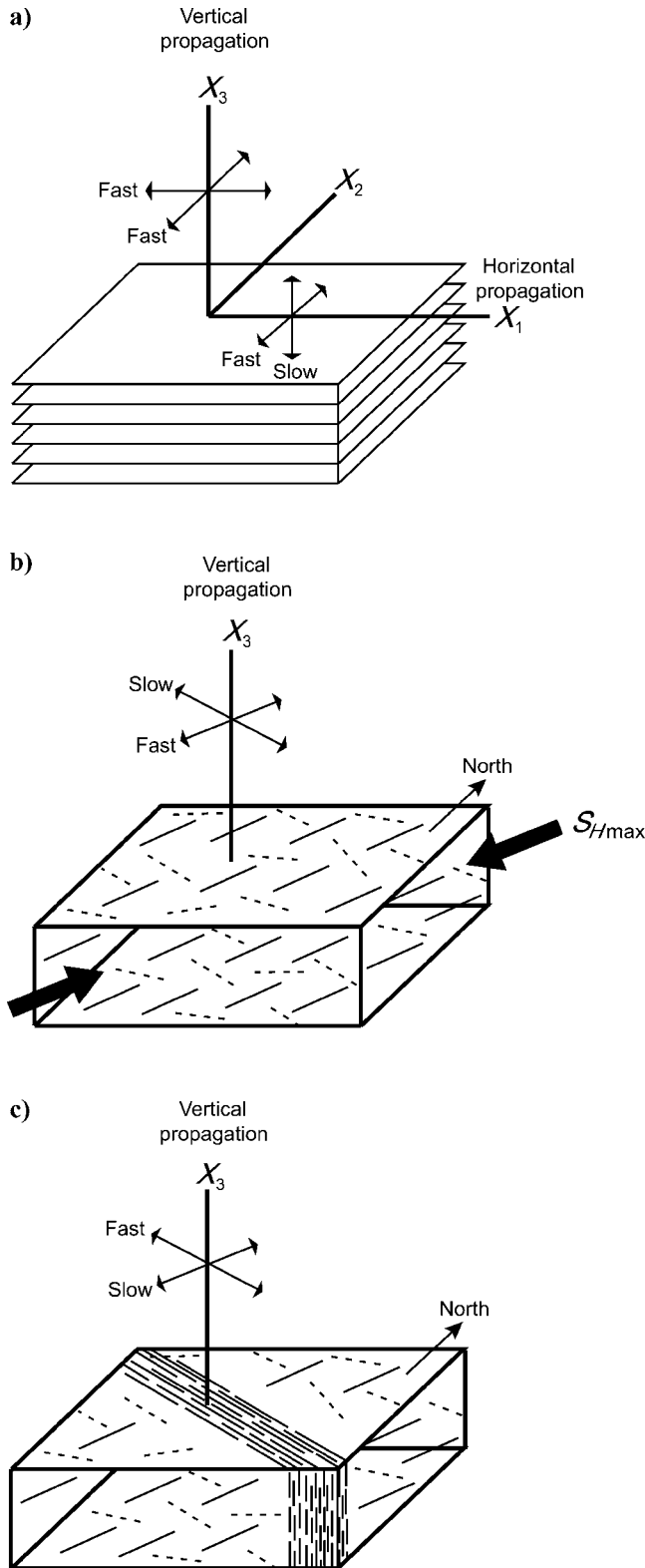
a)

b)

c)

Figure 1. (a) Transverse isotropy associated with subhorizontal bedding for vertically and horizontally propagating shear waves. (b) Transverse isotropy in the context of stress-induced anisotropy as a result of the preferential closure of fractures in a randomly fractured crust. (c) Structural anisotropy as a result of aligned planar features such as the fabric within a major fault zone, sedimentary bedding planes, or aligned minerals/grains.

and perpendicular to the planes normal to the formation symmetry axis (Thomsen, 1986).

Data from the San Andreas Fault Observatory at Depth (SAFOD) drilling project in Parkfield, California, provide the opportunity to study shear velocity anisotropy in the context of physical properties and stress conditions at a variety of scales. SAFOD consists of two boreholes: (1) a vertical pilot hole drilled in 2002 to a depth of 2200 m at a distance of 1.8 km southwest of the surface trace of the SAF and (2) a main borehole (immediately adjacent to the pilot hole) drilled during 2004 and 2005. At the surface, the main borehole is only 7 m from the pilot hole. It remains essentially vertical to a depth of approximately 1500 m before deviating from vertical at an angle of 54°–60° to the northeast toward the SAF to a total vertical depth of 3000 m (Figure 2). A seismic array consisting of 32 three-component (3-C) seismometers was installed in the pilot hole between 800 and 2000 m, and microearthquakes were recorded on 25 of the seismometers from August 2002 to August 2004.

The structural fabric in the Parkfield region is dominated by the northwest-southeast trend of the right lateral strike-slip SAF and associated subparallel strike-slip and reverse faults (Figure 3). Parkfield is located on the transition zone between the 300-km-long locked portion of the fault to the southeast that ruptured during the
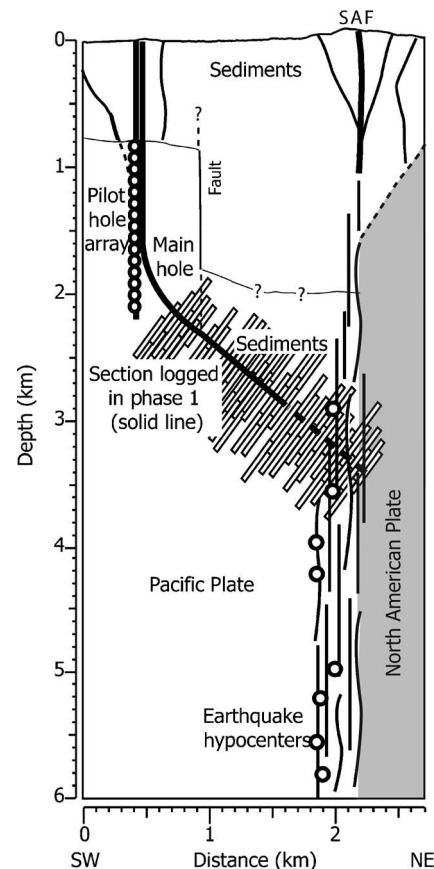

Figure 2. Scaled drawing in the southwest-northeast plane (perpendicular to the SAFOD trajectory), with the SAFOD main borehole and pilot-hole array superimposed on the simplified geology of the North American and Pacific plates separated by the SAF, showing the section of the main borehole where logs were acquired (bold line). The southwest extent of the sediments corresponds with a measured depth in SAFOD of 1920 m, but the depth extent of the lower sedimentary sequence is unconstrained.

great earthquake of 1857 and the creeping section to the northwest. The Parkfield segment of the SAF in central California is of particular interest because of seven historical magnitude-six earthquakes (Bakun and McEvilly, 1984; Roeloffs and Langbein, 1994), including the event that occurred in September 2004.

Regional in-situ measurements of S_{Hmax} at a high angle to the SAF (Mount and Suppe, 1987; Zoback et al., 1987; Townend and Zoback, 2001, 2004) and the absence of a frictionally generated heat-flow anomaly (Brune et al., 1969; Lachenbruch and Sass, 1980; Williams et al., 2004) indicate that the SAF is a weak fault slipping at low shear stress. Measurements of stress orientation in the SAFOD pilot hole indicate S_{Hmax} rotates with depth to become nearly fault normal at depth (Hickman and Zoback, 2004). However, the pilot hole is 1.8 km from the SAF, and the orientation of S_{Hmax} close to the fault is inherently difficult to measure with techniques such as focal mechanism inversion; so it remains somewhat unclear whether far-field stress observations are representative of the physical conditions along the fault plane. We suggest that stress-induced anisotropy measured in SAFOD may provide further constraints on the stress field close to the SAF where other techniques have limitations.

Parkfield is a good natural laboratory for studying the physical mechanisms controlling seismic velocity anisotropy because the northeast orientation of S_{Hmax} is at a high angle to the structural fabric (Figure 3), thus allowing us to distinguish between structural and stress-induced anisotropy in a manner similar to Zinke and Zoback (2000). However, whereas Zinke and Zoback were restricted to microearthquake data recorded at single 3-C seismometers at the surface, we present observations of stress-induced seismic velocity anisotropy recorded in SAFOD at depth. These data are in the immediate proximity of the SAF and supplement previous stress measurements from borehole breakouts and focal mechanism inversions, providing further data on the strength of the SAF.

We are also interested in how observations of anisotropy at both sonic and seismic frequencies at different scales of investigation correlate with physical properties, lithology, and the state of stress inferred from borehole measurements and regional geophysical studies. In particular, the frequency dependence of shear anisotropy may contain useful information regarding the scale of the heterogeneities affecting the shear waves.

To investigate the fine-scale controls on shear-wave velocity anisotropy, we present an integrated analysis of dipole sonic logs in both boreholes from 600–3000 m depth. We correlate the sonic observations with a comprehensive suite of geophysical logs, including sonic-velocity, resistivity, gamma-ray, and porosity logs; an analysis of macroscopic fractures using the electrical conductivity image logs; and geologic analyses of cuttings/core. The sonic logs are investigating the anisotropy of the rocks at a scale of a few meters around the borehole, but we also present shear-wave-splitting measurements at seismic wavelengths for nine microearthquakes recorded on the pilot-hole array that sample a volume of the crust on the order of about 8 km³.

LITHOLOGY AND PHYSICAL PROPERTIES

In this section we present an integrated analysis of data acquired in the SAFOD pilot hole and phase one of the main borehole to a depth of 3050 m to determine the formations intersected by the SAFOD boreholes. The data set includes petrophysical logs (Figure 4), electrical conductivity formation microimager (FMI), used by Schlumberger image logs (Figures 5 and 6), and thin-section analy-

sis of rock cuttings collected every 3 m during drilling. Real-time gas measurements (T. Wiersberg, personal communication, 2005) were used to identify hydraulically conductive intervals that possibly correspond to faults/fractures or more permeable sedimentary units. Note that all depths are measured depths along the borehole trajectory and are referenced to the main hole's kelly bushing at 10 m above ground level (measurements in the pilot hole are also corrected to this depth reference).

Tertiary and Quaternary sediments were encountered to a depth of 780 m above granite and granodiorite, the expected basement rock of the Salinian terrane west of the SAF. The vertical pilot hole (Figure 2) then remained in Salinian granite to a depth of 2200 m. However, after kicking off toward the SAF (Figure 2), the main borehole penetrated a major fault zone at 1920 m (230 m northeast of the kickoff from vertical), below which a sequence of sedimentary rocks was encountered. The sedimentary sequence mostly consisted of packets of alternating sandstone and siltstone with intervals of finely laminated shale, some with conglomeritic clasts. A 12-m core sample was obtained at the bottom of phase one between 3055 and 3067 m depth, composed of well-cemented arkosic sandstones and fine siltstones with numerous fractures and faults (Almeida et al., 2005).

The petrophysical logs (sonic velocity, resistivity, gamma ray, density, and neutron porosity) were used to characterize the lithologic units penetrated by the main borehole. In the pilot hole, three major shear zones at 800, 1400, 1920, and 2550 m were identified with anomalous physical properties: low sonic velocity, low resistivity, high gamma ray, changes in porosity, increased fracturing on the FMI log, and increased gas emissions (Boness and Zoback, 2004).
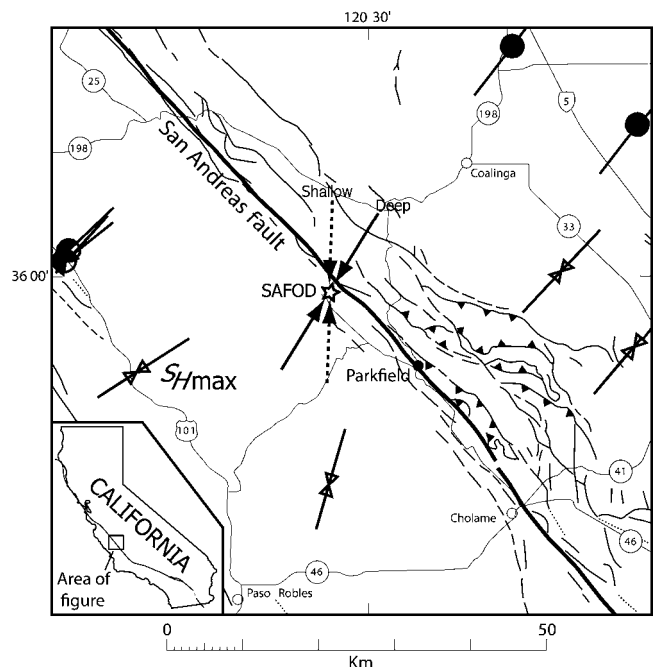

Figure 3. Location of SAFOD, 1.8 km southwest of the SAF in central California. The orientation of the maximum horizontal compressive stress S_{Hmax} from focal mechanism inversion (circles) and wellbores (bowties) (data from World Stress Map) is at a high angle to the northwest-southeast trend of the structural fabric. In the SAFOD pilot hole, shallow and deep measurements of S_{Hmax} (Hickman and Zoback, 2004) indicate a clockwise rotation with depth to more fault-normal compression.

However, within the lower suite of sedimentary rocks, it was difficult to distinguish between shale units and shear zones using the geophysical logs because they have very similar physical properties.

The upper granitic section of the SAFOD main hole is characterized by physical properties similar to those reported in the pilot hole by Boness and Zoback (2004). As shown in Figure 4, the compressional and shear sonic velocities (V_p and V_s) generally increase with depth, although there are many high, short-wavelength intervals of lower velocity associated with minor fractures. At the base of the granodiorite in the main borehole, both V_p and V_s show a marked decrease leading into the major fault located at 1920 m, probably indicating a fault-damage zone. Overall, the resistivity increases from 10 ohm-m in the Tertiary sediments to a maximum of 500 ohm-m in the granodiorite. Interestingly, the resistivity also shows a decrease from 1800 to 1920 m down to 90 ohm-m before showing a major

decrease to 10 ohm-m in the fault separating igneous and sedimentary units at 1920 m. The natural gamma-ray log shows an increase from about 50 °API in the granite to about 100 °API in the granodiorite, probably reflecting the increase in felsic minerals such as plagioclase feldspar.

Density and neutron porosity in the granite appears to be very high in some intervals from 820–1050 m. However, the four-arm caliper data indicate this section of the hole is washed out, and we suggest these are erroneous measurements caused by hole enlargement in these intervals. Below 1050 m where the hole is in gauge with respect to bit size, the density and neutron porosity logs agree and indicate a porosity of about 10%. Porosity measurements of a granite sample from the pilot hole reveal a matrix porosity of 1%–2%. We attribute the higher bulk porosities observed in the density and neutron porosity logs to the result of pervasive in-situ macroscopic fractures that are not present in the small, intact core sample. An analysis of the FMI logs in both the main hole and pilot hole (Figure 5) indicates an average fracture density of 30 fractures per 10-m interval. However, the number of fractures visible in the image logs from the main hole is approximately one-third less than in the pilot hole on account of poor image quality; the FMI tool has less coverage in the larger diameter main hole.

In Figure 5, the orientations of the fractures are shown as poles to fracture planes on lower-hemisphere stereonets and as rose diagrams where the size of each 5° petal is proportional to the number of fractures with a strike orientation within that bin (relative to north pointing upward). The rose diagrams in particular illustrate the highly variable orientations of fractures and the lack of correlation with measurements of S_{Hmax} in the pilot hole. In addition, many of the fractures are low angle, and the significance of these more ambiguous strike directions is overrepresented by the rose diagrams. There is also a sampling bias as a result of the orientation of the borehole, which prohibits the observation of fractures that are parallel to the borehole trajectory. This phenomenon is evident in the stereonets in Figure 5 by an absence of fracture poles in the 90° halo around the average borehole trajectory (red cross) within each interval.

In addition to visual analysis of the fracture orientations using stereonets, we also use directional statistics designed to determine clusters of directional data in an objective way. Objective grouping of the data is performed by optimizing the mean pole vector that describes the fractures within each 200-m interval (Anderberg, 1973). An orientation matrix is computed for the fractures in each depth interval, and the optimal orientation of the mean value is found by principal component analysis of the orientation matrix (Kiraly, 1969; Darot and Bouchez, 1976). We compute the normalized maximum eigenvalue and corresponding eigenvector, which represents the principal direction of the fractures. The eigen-
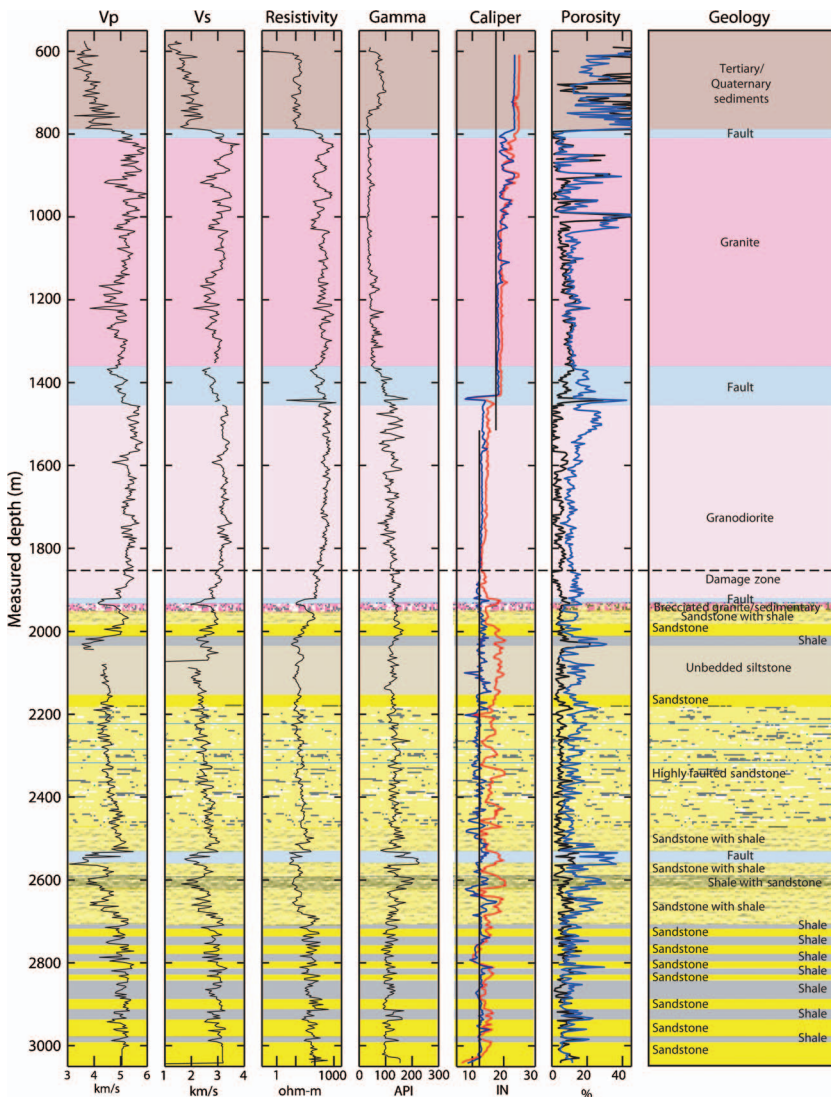

Figure 4. Petrophysical logs collected in the SAFOD main borehole, used in conjunction with electrical conductivity image logs, real-time gas observations, and cuttings analysis to determine the lithologic profile. The caliper has four arms, giving two orthogonal measurements of the borehole diameter. Two measurements of porosity are shown: density porosity (in black), determined from the density log using a reference grain density of 2.65 g/cm³, and neutron porosity (in blue), which reflects the amount of bound water in the formation. The red curve indicates the nominal borehole diameter.

vectors are described by a strike and dip, which characterizes the properties of the fracture clusters within the interval. Eigenvalues range from 0–1, where zero indicates complete statistical randomness of fracture orientations and one indicates that all fractures within the interval have exactly the same orientation. For the fractures intersected by the SAFOD boreholes, the maximum eigenvalues for each interval are 0.2–0.56, indicating limited preferential direction of the macroscopic fractures.

The depth range with the most preferential orientation of fractures is 1600–2000 m in the main hole, with a fairly consistent northnorthwest strike direction. However, the same interval in the pilot hole is only a lateral distance of less than 400 m away and does not show the same consistent pattern. Below 1500 m the borehole trajectory is highly deviated, and the lack of consistency between mainhole orientations and the highly variable pilot-hole orientations suggests a sampling bias caused by the differing hole deviations. The sedimentary section was first intersected by the main hole at a measured depth of 1920 m; we postulate that between 1800 and 2000 m, some of the linear features in the FMI log interpreted to be fractures are actually sedimentary bedding planes, explaining the degree of correlation in the strike direction.

The orientation of S_{Hmax} in the pilot hole as determined by Hickman and Zoback (2004) using wellbore breakouts and drilling-induced tensile fractures is also shown for reference on the stereonets. Little correlation between the fractures and stress orientation is observed (Boness and Zoback, 2004).

Below the granodiorite, the SAFOD main hole encountered a sedimentary sequence of rocks, consisting primarily of arkosic sandstones, shales, and siltstones. In general, the sonic velocities are only slightly lower than those measured within the granite above, with V_p from 4.2–5.4 km/s and V_s from 2.2–3.2 km/s; both show an overall increasing trend with depth. Similarly, the resistivity in the sedimentary rocks increases with depth.

The gamma-ray log in the sedimentary units is very similar to the measurements within the granodiorite and remains fairly high, which makes sense, given the arkosic composition of the sandstones that are rich in potassium feldspar and the clay-rich shales. Within some fault zones (e.g., 2550 m) the gamma-ray log exhibits a local high, perhaps from an increase in clay content and enrichment of mobile radioactive elements (potassium, uranium, thorium). However, the major fault that juxtaposes granite and sedimentary rocks at 1920 m does not have a distinct gammaray signature.

Porosity derived from density measurements is fairly consistent throughout the sedimentary section at about 10%. However, the neutron porosity log, which is sensitive to hydrous mineral phases in addition to free water, is much more variable and increases from a background level of approximately 10% to a maximum of approximately 40%. Although there are clear overall trends in all

of the physical properties with depth throughout the sedimentary sequence, we have identified a number of discrete sandstone and shale units characterized by obvious deviations from average properties.

The sandstone units are characterized by higher velocities and resistivity, low gamma-ray readings, and slightly lower density and neutron porosity values than the other sedimentary units. An analysis of the cuttings samples in thin section reveals that these are arkosic sandstone units, composed of angular grains of granitic origin that have been well-cemented together (D. Moore, personal communication, 2005). We discriminate bedding planes from fractures on the FMI log by looking for intervals of very consistently striking and dipping planes that are regularly spaced. The orientation of bedding planes is shown in Figure 6.

Within the sandstones, bedding planes are observed on the FMI image log at regularly spaced intervals of 0.5–2 m. In contrast, there are many shale intervals associated with decreased velocity, decreased resistivity, and increased gamma-ray and neutron porosity values. In these intervals, thin-section analyses (D. Moore, personal
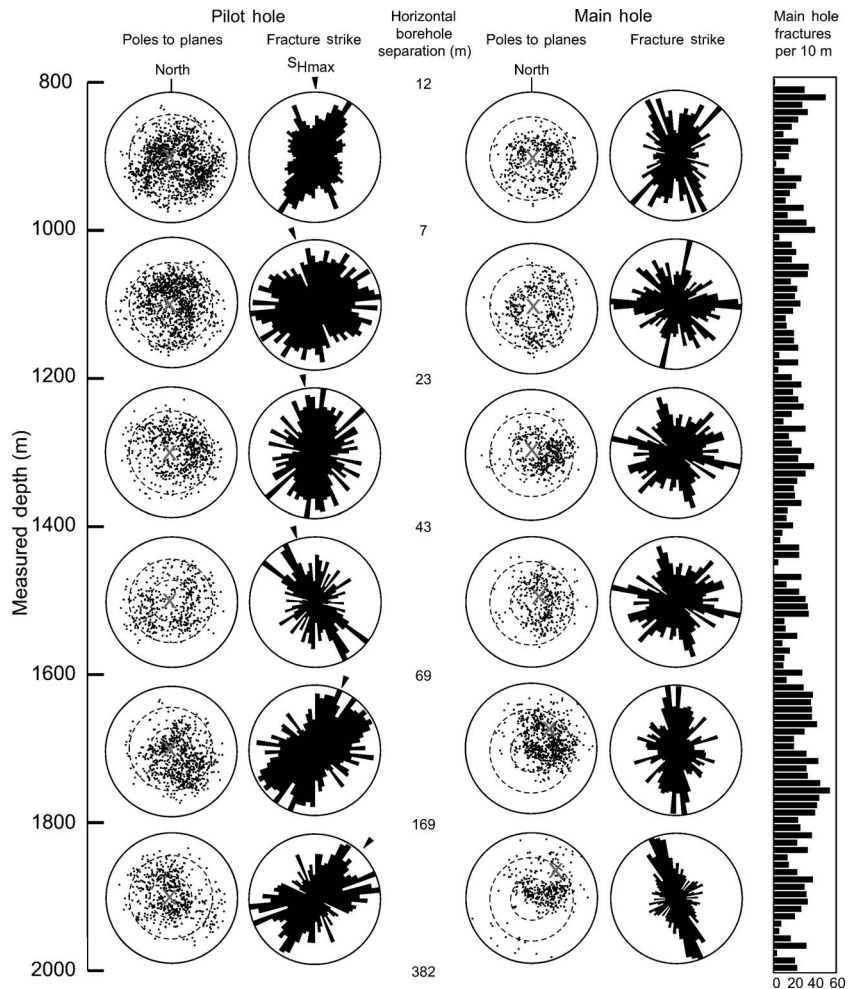

Figure 5. Lower-hemisphere stereographic projections of poles to fractures, and rose diagrams of fracture strike determined from the electrical conductivity image logs in the granitic section of both the pilot hole and main hole at 200-m intervals. The trajectories of the pilot hole and main hole are shown as red crosses on the stereonets, and the dashed circles represent dips of 30° and 60° for reference. The measurements of S_{Hmax} in the pilot hole are shown for reference as black triangles on the rose diagrams. The lateral distance between the boreholes at each depth is also shown. The histogram depicts the number of fractures per 10 m observed in the SAFOD main hole.

communication, 2005) and X-ray diffraction analysis of the cuttings (J. Solum, personal communication, 2005) indicate an increase in clay minerals and sheared grains relative to the sandstones. The FMI image log reveals that these intervals are also characterized by a very conductive granular fabric with the presence of small resistive clasts. The bedding in these intervals is difficult to discern on the FMI image log amid the conductive matrix; but where it is visible, it shows a much tighter spacing than the sandstone units and may be better described as finely laminated (Figure 6).

We interpret these intervals to be conglomeritic shale similar to the three Cretaceous debris flow deposits found in the Great Valley sequence in the general vicinity of Parkfield. The Juniper Ridge conglomerate is the uppermost of these channel levee units and is found in outcrop slightly west of Coalinga, interbedded with thick-bedded sandstones, mudstones, and shales (Hickson, 1999; Hickson and Lowe, 2002). However, as noted above, we cannot rule out the possibility that some of these shale layers may be faults.

One other unit of interest is the siltstone found at approximately 2000 m. This siltstone is characterized by intermediate velocities and resistivity but is known from drilling to contain oxidized iron minerals, causing it to be very red. The bedding in this interval, when visible in the FMI image log, is finely laminated and reminiscent of the thin, fine-grained muddy turbidites deposited in the Great Valley during periods of low sediment influx (Lowe, 1972).

In all of the units, the bedding planes strike nearly parallel to the surface trace of the SAF, and the majority dip away from the SAF to the southwest with an average dip of 39° (Figure 6), although increasingly more beds dip to the northeast near the bottom of the borehole. The opposite sense of dip (to both the southwest and northeast) within different intervals of the sedimentary sequence may indicate folds associated with the transpressional (simultaneous occurrence of strike-slip faulting and compression) nature of this tectonic region or faults separating distinct blocks. Most of the observed bedding planes are essentially perpendicular to the borehole trajectory of SAFOD.

SHEAR ANISOTROPY MEASURED WITH DIPOLE SONIC LOGS

Data from open-hole dipole sonic shear logs are used to assess shear-wave velocity anisotropy at sonic frequencies (Kimball and Marzetta, 1984; Chen, 1988; Harrison et al., 1990). In the pilot hole a Dipole Sonic Shear Imager (DSI as named by Schlumberger) log was acquired in 2002, and in the main borehole a Sonic Scanner log (Schlumberger tool) was obtained in 2004. The sonic scanner and DSI are multireceiver tools with a linear array of 13 and 8 receiver stations, respectively, spaced at 6-inch intervals (Schlumberger, 1995). On the sonic scanner each receiver station consists of eight azimuthal receivers; the DSI has four receivers, resulting in 104 and 32 waveforms, respectively, for each dipole firing with which to compute shear velocity anisotropy. The transmitter on these dipole sonic tools is a low-frequency dipole source operating from 0.8–5 kHz frequency (Schlumberger, 1995). A dispersive flexural wave propagates along the borehole wall with a velocity that is a function of the formation shear modulus. At low frequencies the flexural-wave velocity approximates the shear-wave velocity and in the case of SAFOD has a depth of investigation of approximately 1.5 m into the formation. The flexural mode is recorded subsequently on the array of receivers.

We define the amount of velocity anisotropy as $100(V_{s1} - V_{s2})/V_s$, where V_{s1} is the fast shear velocity, V_{s2} is the slow velocity, and V_s is the mean shear velocity. We use three quality control (QC) measures to ensure the dipole shear-wave data are reliable: (1) velocity anisotropy greater than 2%, (2) a difference of more than 50% between the minimum and maximum of the crossline energies (Esmersoy et al., 1994), and (3) a minimum crossline energy of less than 15% after rotating the waveforms into the fast and slow directions (Alford, 1986).

Stress concentrations attributable to the presence of the borehole are expected to exist around the wellbore to distances of up to approximately three borehole radii (Jaeger and Cook, 1979). The dispersive nature of the flexural wave (Figure 7) is used to filter out the high frequencies corre-
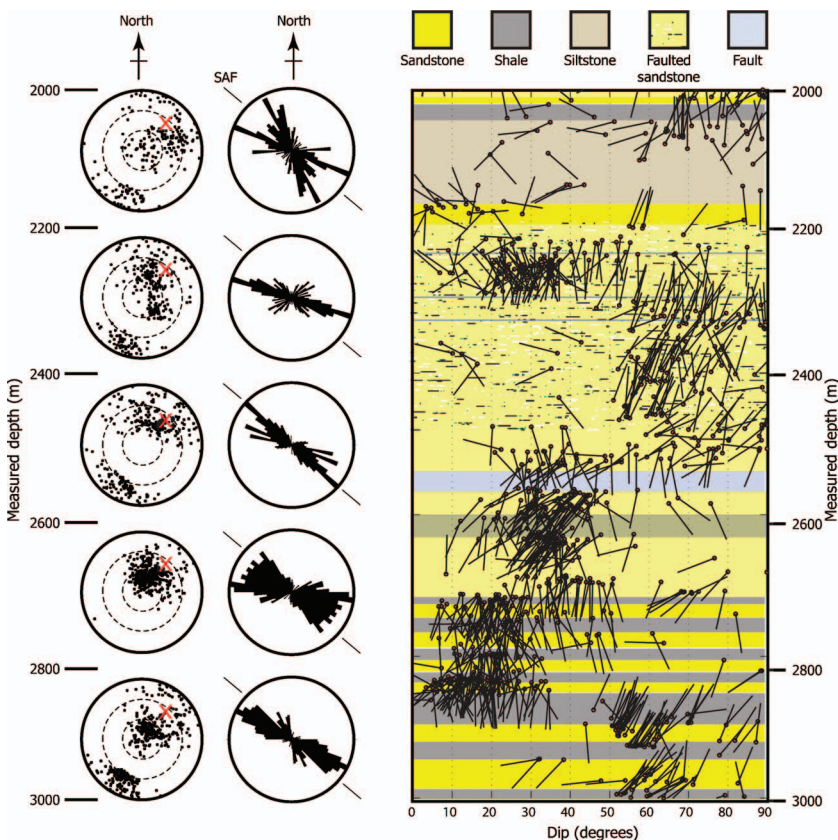

Figure 6. Bedding planes in the sedimentary sequence between 2000 and 3000 m, intersected by the main hole from electrical conductivity image log analysis over 200-m intervals. Stereonets show the poles to planes of all planar features, and rose diagrams emphasize the strike of the beds. The trajectory of SAFOD is shown with a red cross on the stereonets, and the strike of the SAF is shown on the rose diagrams for reference. A tadpole plot is overlain on the sedimentary lithology with a point indicating the dip of each bed and the tail pointing in the dip direction.

sponding to short wavelengths that sample the rocks subjected to the stress concentration around the borehole (Sinha et al., 1994). The observations presented here are the shear velocities that correlate with low frequencies (usually less than about 2 kHz) and therefore long wavelengths that penetrate deep into the formation beyond the altered zone around the wellbore.

In addition, borehole ovality biases the results of a shear-wave-splitting analysis with dipole sonic logs (Leslie and Randall, 1990; Sinha and Kostek, 1996). The dispersion curves of the rotated fast and slow waveforms indicate apparent anisotropy from borehole ovality when the shear-wave velocity shows no separation at either high or low frequencies but demonstrates a significant split into fast and slow velocities at midrange frequencies (Figure 7). In theory, the lack of separation between the shear velocities at low frequencies means that anisotropy as a result of borehole ovality would automatically be removed in the QC procedure described above. However, in the main hole there are numerous examples where the caliper data indicate an enlarged hole and the shear waves do not always show typical behavior at low frequencies. By analyzing the dispersion curves at every depth interval, we could remove all cases where borehole ovality affects anisotropy.

Also, studies show that the fast and slow dispersion curves exhibit a crossover in the presence of stress-induced anisotropy (Winkler et al., 1998), which would provide valuable information regarding the cause of the anisotropy. However, the overall quality of the SAFOD data set is insufficient to assess the crossover phenomenon with any accuracy.

DIPOLE SHEAR ANISOTROPY IN SAFOD

After applying the QC measures to the dipole sonic data collected in the SAFOD boreholes, we project the fast polarization directions observed in the deviated section of the borehole onto a horizontal plane so they may be compared directly with fast directions in the vertical section of the borehole. We then compute the mean fast direction of the shear waves over 3-m intervals. We choose Bingham statistics (Fisher et al., 1987) to compute the mean because the fast directions are of unit amplitude (i.e., they are not vectors). The normalized eigenvalues (computed in the same way as for fractures) give a measure of the relative concentration of orientations about the mean, and we discard any mean fast direction over a 3-m interval with a normalized eigenvalue of less than 0.9.

The upper vertical section of the main hole essentially overlaps with the pilot hole, and we choose to use the seismic velocity anisotropy results from the pilot hole within this depth interval (700–1500 m) because the borehole is smaller and has fewer washouts, so the sonic tool is better centered within the hole. However, a comparison of both logs indicates a high level of repeatability. The combined dipole sonic anisotropy results from both holes are shown in Figure 8.

Within the granite, from 760–1920 m, the fast polarization direction of the shear waves is approximately north-south and exhibits a rotation to a more northeasterly direction with depth. The amount of anisotropy decreases from about 10% at the top of the granite to approximately 3% at the bottom of the granodiorite. Three distinct intervals exist within the granite, where the amount of anisotropy is observed to increase by up to 10% above the overall trend in both the pilot hole and the main borehole. The depths of these intervals in the pilot hole are reported by Boness and Zoback (2004) as 1150–1200 m, 1310–1420 m, and 1835–1880 m. In the main bore-

hole we observe increases in the amount of anisotropy at 1050–1100 m, at 1360–1455 m, and at the granodiorite-sediment interface at 1920 m. It is relevant that in both the pilot hole and main borehole, the fast polarization direction within these intervals remains consistent with the fast direction throughout the rest of the granite, even though the amount of anisotropy increases.

Above a depth of 1920 m, in both the pilot hole and main hole, the faults and fractures observed on the image logs show no preferential orientation (Figure 5). However, the direction of S_{Hmax} from a wellbore failure analysis in the pilot hole (Hickman and Zoback, 2004) as shown in Figure 8 illustrates the remarkable correlation between fast polarization direction and stress within the granitic section. The seismic anisotropy is interpreted to be stress induced, caused by the preferential closure of fractures in response to an anisotropic stress state (Boness and Zoback, 2004). Further evidence for stress-induced anisotropy is that the amount of velocity anisotropy decreases with depth in the granite section of the borehole from approximately 10% at 780 m, to 3% at 1920 m (Figure 8). We interpret this decrease to be the result of increased confining pressure with depth, which tends to close fractures in all orientations and thus makes velocity anisotropy less stress sensitive at higher pressure (e.g., Nur and Simmons, 1969).

The zones in the granite where the amount of anisotropy in the
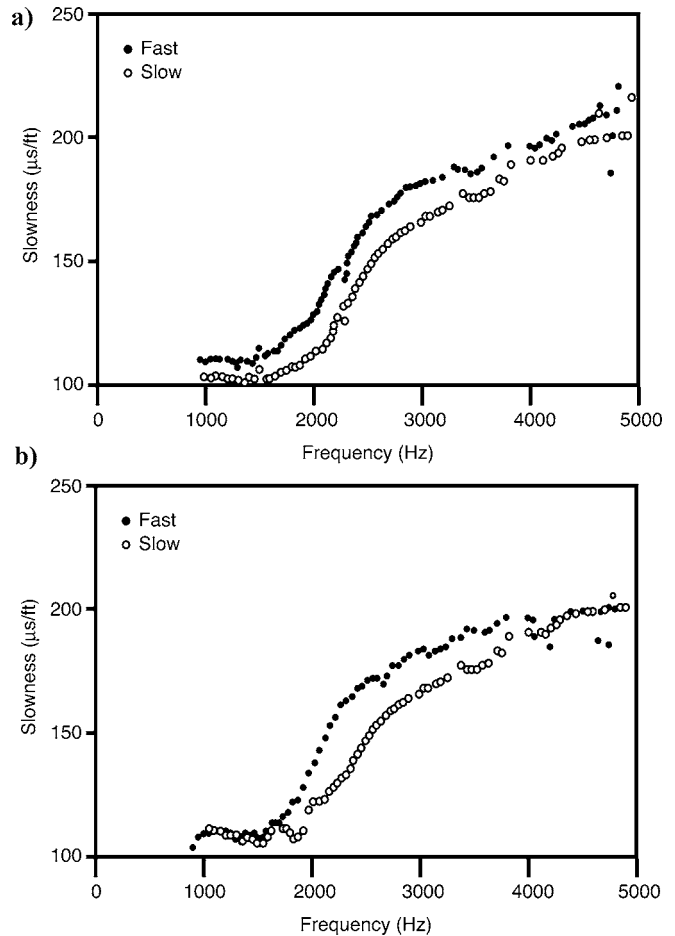
Figure 7. Example of dispersion curves for rotated waveforms used to distinguish between (a) formation anisotropy and (b) anisotropy caused by borehole ovality.

sonic log increases by up to 10% above the overall trend correlate with intervals of anomalous physical properties (e.g., low sonic velocity, low resistivity, high gamma-ray readings, increased fracturing). As discussed in detail by Boness and Zoback (2004), these intervals are intensely fractured but do not exhibit borehole breakouts, which is curious, considering that the low velocity would imply lower rock strength. These intervals are interpreted to be shear zones with low shear stress, probably resulting from past slip events on faults. The high amounts of velocity anisotropy within the shear zones are inferred to be the result of the increased sensitivity of seismic velocity at low mean stress (e.g., Nur and Simmons, 1969) or of enhanced microcracking (Moos and Zoback, 1983).

The fact that the fast shear waves are polarized parallel to the stress in the shear zones leads us to believe this is not structural anisotropy but instead is related directly to perturbations in the stress state. It is well known that fault zones are often associated with a rotation of $S_{H\max}$ and a localized absence of breakouts (Shamir and Zoback, 1992; Barton and Zoback, 1994). Interestingly, we observe westerly rotations in the fast direction of the shear waves over depth intervals of approximately 100 m just below the major shear zones

at 800, 1400, and 1920 m. The rotation in fast directions is below the shear zones, whereas the gradual change in physical properties that we interpret to be a damage zone appears to lead into the shear zones from above.

At the transition from granite to sedimentary lithology at 1920 m, Figure 8 illustrates that the amount of velocity anisotropy significantly increases to an average value of about 6%, which remains approximately constant to the bottom of the hole but has a number of fluctuations on the order of ±2%. The change in lithology from granite to sedimentary rocks occurs just below the depth at which the SAFOD borehole begins deviating toward the San Andreas fault. This presents an obvious challenge for separating out the effects of geology and well slope on the anisotropy and is one of the objectives of this paper. Within the sedimentary section (1920–3000 m), there are two trends in the fast polarization directions of the shear waves: a northwest orientation (red dots on Figure 8) and a northeast orientation (blue dots) consistent with the fast directions in the granitic upper section. We correlate the fast polarization directions with lithology and petrophysical properties and model the observations of shear anisotropy, taking into account the borehole deviation and the orientation of the formation bedding planes. In many places, the orientation of the bedding planes is nearly orthogonal to the wellbore; however, if the bedding planes were exactly perpendicular, then no structural anisotropy would be detectable. Thus, even though the amount of anisotropy may be diminished with this geometry, if any anisotropy is observed, the fast azimuth of the shear waves still contains useful information about the formation. We propose that both stress and lithologic structure are dominant controls on the anisotropy we observe.

To further our understanding of the structural anisotropy within the sedimentary section, we consider the FMI log from 2000–3000 m in discrete intervals of 10 m and compute the mean bed orientation (dip direction and strike) using Fisher vector distribution statistics (Fisher et al., 1987). We discard all intervals with less than four beds or with a normalized mean eigenvalue of less than 0.9. After computing the mean bed orientations, we use the theoretical formulation in Appendix A to compute the apparent fast direction for each discrete 10 m interval that would be observed in the SAFOD borehole if the shear waves were being polarized with a fast direction parallel to the bedding planes. Between 2000 and 3000 m, the borehole has an average azimuth and deviation from vertical of 35° and 54°, but a gyroscopic survey is used to input the exact borehole azimuth and inclination at each depth interval. In Figure 9 we show the number of bedding planes used to compute the mean orientation and compare the theoretical apparent fast direction with the fast direction observed on the dipole sonic tool.

Figure 9 shows that within the well-cemented (high seismic velocity), massively bedded sandstones (2170–2500 m), the sonic log exhibits a northeast fast polarization direction, consistent with observations in the granite at shallower
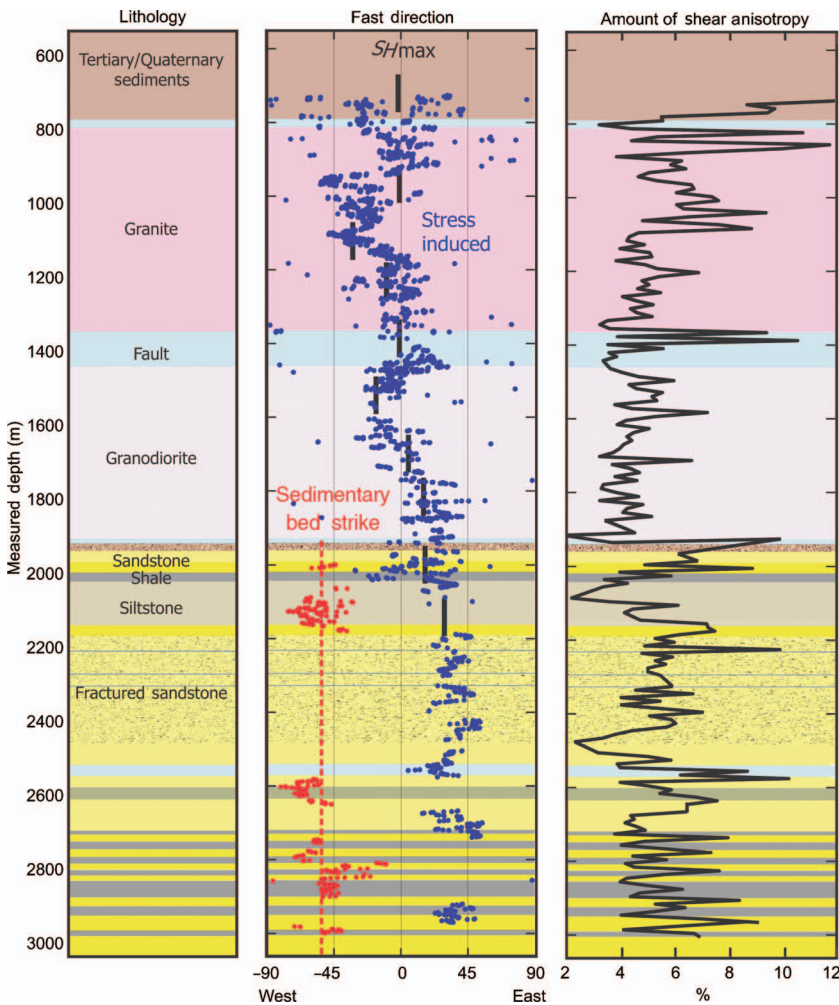

Figure 8. Observations of shear velocity anisotropy from the dipole sonic logs in the pilot hole (700–1500 m) and main hole (1500–3050 m). The direction of the sedimentary bedding planes (red dashed line) is the mean strike determined in the electrical conductivity image. The black bars in the middle plot indicate the orientation of $S_{H\max}$ in the pilot hole.

depths but which do not correlate with the theoretical fast directions if bedding planes were polarizing the shear waves. However, in the finely laminated, clay-rich shale and siltstone units below 2550 m, the northwest fast direction of the sonic shear waves generally correlates well with the theoretical fast directions for structural anisotropy. We interpret the seismic anisotropy within these finely bedded stratigraphic layers to be controlled by the alignment of clay and mica platelets in the strike direction of the bedding planes. The FMI log indicates that the bedding within most of the sandstone units is spaced at much larger intervals — about (0.5–2 m). The spacing of these bedding planes is comparable to the 1.5 m wavelength of the sonic waves at the low frequencies of interest, which explains why we only observe structural anisotropy within the shale despite the subparallel bedding planes present within all sedimentary units.

The lack of correlation between the theoretical predictions for structural anisotropy and the observations in the well-cemented sandstones suggests stress-induced anisotropy in these units. The geometry of the borehole relative to the maximum compressive stress will dictate the amount of anisotropy observed (Sinha et al., 1994). The fast direction is found by rotating the sonic-log waveforms until the maximum and minimum energy levels are found at the time of the shear wave's arrival (Alford, 1986; Esmersoy et al., 1994), so the accuracy of the measurement is diminished when there is less anisotropy.

Assuming the observed anisotropy occurs because S_{Hmax} preferentially closes fractures, the 54° inclination of SAFOD will reduce the amount of stress-induced anisotropy observed by up to approximately 50% (Sinha et al., 1994). Of course, this depends on the magnitudes of the other two principal stresses. However, in the sedimentary section of SAFOD, the observed amount of anisotropy exceeds 4%, so we believe the fast direction is a robust measurement. We cannot rule out that some of the anisotropy observed in the deviated section of the borehole is partly a result of fractures being closed preferentially by the vertical stress S_v. However, the plane perpendicular to the borehole is at approximately 45° to both S_{Hmax} and S_v. But because this is a strike-slip/reverse stress regime, S_{Hmax} is larger, and it is unlikely that S_v is a dominant stress polarizing the shear waves.

PILOT-HOLE ARRAY

In 2002, an array of 32 3-C, 15-Hz seismometers was installed in the granitic portion of the pilot hole between 850 and 2050 m depth (Chavarria et al., 2004). Data from this array are well suited for a shear-wave-splitting analysis because the high sampling frequency (2 kHz) allows us to pick the onset of the shear waves accurately. We analyze seismograms from nine local microearthquakes at the 25 seismometers that were operational in the pilot hole during the events. The earthquakes analyzed in this study are located on the SAF approximately 1.5 km laterally to the northeast and between depths of 2.7 and 7.3 km (Figure 10). The events were chosen be-

cause they had particularly well-constrained relocations (J. A. Chavarria, personal communication, 2005), were distributed laterally along a limited 4-km along-strike section of the SAF, and had especially high S/N ratios with impulsive shear-wave arrivals. The waveforms used in this study arrived at the array receivers at incidence angles of less than 40° within the shear-wave window (Nuttli, 1961; Booth and Crampin, 1985), minimizing the likelihood of contamination from converted phases. The shear-wave energy peaked at 20 Hz, so we filtered the seismograms using a Butterworth bandpass filter with 5–35-Hz limits.

The shear-wave-splitting analysis was conducted using a technique that combines the methods of Silver and Chan (1991) and Zhang and Schwartz (1994). We used a grid search to find the values of fast polarization direction and the time delay between the split shear waves that best corrected the seismograms for the effects of anisotropy. The recorded seismograms were rotated into an earthquake reference frame, the particle motion of the S_H and S_V waveforms was plotted on a hodogram, and the shear-wave arrival was determined by looking for an abrupt change from linear to elliptical particle motion. The seismograms were windowed around the shear-wave arrival with 0.2 s before the shear-wave arrival and 0.5 s after. For orthogonal shear-wave displacement vectors $\mathbf{u}_1$ and $\mathbf{u}_2$ (usually direc-
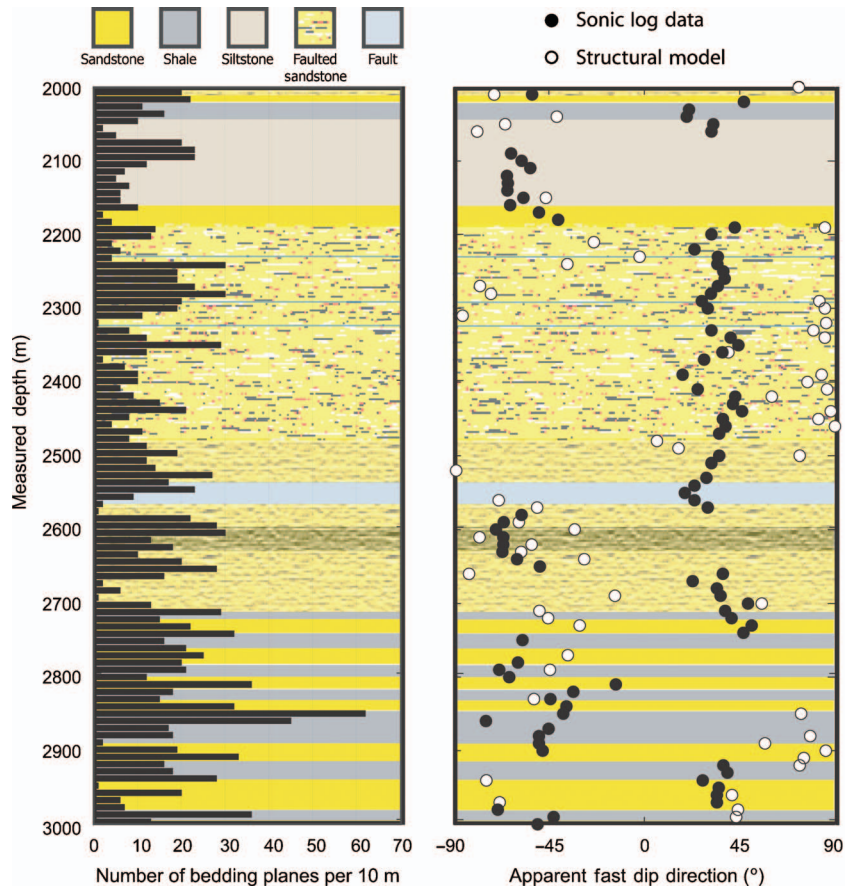

Figure 9. Histogram showing the number of bedding planes per 10-m interval used to compute the mean bed orientation using Fisher statistics, and comparison of observed fast directions from the sonic logs with the theoretical apparent fast direction that would be observed assuming the fast direction is oriented along the bedding planes, overlain on the lithology.

tions 1 and 2 refer to north-south and east-west), the covariance matrix of the particle motion is computed by

$$c_{ij}(\alpha, \delta t) = \int_{-\infty}^{\infty} u_i^{\alpha}(t) u_j^{\alpha}(t - \delta t) dt \quad i, j = 1, 2, \quad (1)$$

where u_l^{α} indicates a horizontal rotation of u_l by α degrees. We searched over values of α in 1° increments from $-90°$ to $90°$ and over delay times δt between 0 and 50 ms in increments of the data time sampling interval of 0.05 ms. If anisotropy existed, c_{ij} had two nonzero eigenvalues λ_1 and λ_2, where λ_1 was the largest (unless $\alpha = n\pi/2$ for $n = 1,2...$). The fast direction and delay time that best linearized the particle motion were determined by minimizing λ_2 of the particle motion covariance matrix. To quantify the accuracy of the measurement, we computed the degree of rectilinearity (Jurkevics, 1988) as

$$r = 1 - \left(\frac{\lambda_1}{\lambda_2}\right). \quad (2)$$

We only reported measurements with a degree of linearity greater than 0.8 (1 being perfectly linear). Once rotated into a fast-slow coordinate system, the fast and slow waveforms should have similar pulse shapes. Following the method of Zhang and Schwartz (1994), we confirmed the fast polarization direction and more accurately determined the delay time by crosscorrelating the windowed seismograms at each rotation step over lags of ± 0.2 s. Silver and Chan (1991) point out that maximizing the crosscorrelation coefficient is similar to minimizing the determinant, so we used the maximum

crosscorrelation coefficient to confirm the seismograms were rotated into the fast and slow polarization directions. We discarded any measurement that had a crosscorrelation coefficient of less than 0.7.

To ensure the highest level of confidence, we only reported the fast polarization direction from the covariance matrix decomposition if the maximum crosscorrelation coefficient were for a rotation azimuth within $\pm 10°$ of this measurement. The maximum uncertainty on the fast polarization directions was therefore estimated to be a maximum of $\pm 10°$. The time delay we documented was from the crosscorrelation procedure and was normalized by the distance along a linear raypath from the source to the receiver. An example of the shear-wave-splitting analysis procedure is shown in Figure 11.

The results of this study using data from the pilot-hole array are shown in Figure 12, plotted at the depth of each receiver. The fast polarization directions are north-northeast in the upper receivers on the array; but below a depth of 1400 m, the fast direction of the shear waves rotates to a northwest orientation. The northeast fast direction observed on the upper receivers corresponds with delay times that decrease with depth from 8 ms/km at the top of the array to 4 ms/km at 1400 m. The fast directions determined on the upper receivers also correlate with the direction of S_{Hmax} determined in the pilot-hole stress analysis (Hickman and Zoback, 2004). The decrease in the amount anisotropy is consistent with stress-induced anisotropy as the confining pressure increases with depth. The northwest fast direction observed on the lower receivers is associated with delay times that show an apparent increase with depth from 4 ms/km at 1400 m up to about 10 ms/km at 2000 m. The observations of shear velocity anisotropy on the lower receivers of the pilot-hole array are inconsistent with stress-induced anisotropy, but the fast polarization directions correlate with the fabric of the sedimentary bedding. The deeper on the array a receiver is, the more relative time the seismic waves spend being polarized by the fault fabric, which accounts for the increasing delay time with depth.

We contend that on these lower receivers, we are observing structural anisotropy. However, it is not intuitive how shear waves generated by a single earthquake can display both stress-induced anisotropy and structural anisotropy at different receivers in the same vertical array. To explain this apparent paradox, we show simplified (i.e., linear) raypaths from the nine earthquakes analyzed to both an upper and a lower receiver in Figure 10. Raypaths to the lower receivers are mostly through the northwest-striking sedimentary bedding, explaining the presence of structural anisotropy observed on the lower receivers. Of course, the depth extent of the sedimentary package is unconstrained, so it is very possible that the lowermost raypaths are also entirely in the sediments. However, it is well known that the amount of anisotropy is cumulative along the raypath but that the polarization direction is controlled by the last anisotropic medium encountered by the wave (e.g., Crampin, 1991). Thus, the lower raypaths, which are in the sediments immediately before being recorded, are polarized by the bedding.

The raypaths to the upper receivers also go through the sedimentary sequence, but the last portion of the raypaths is through the fractured
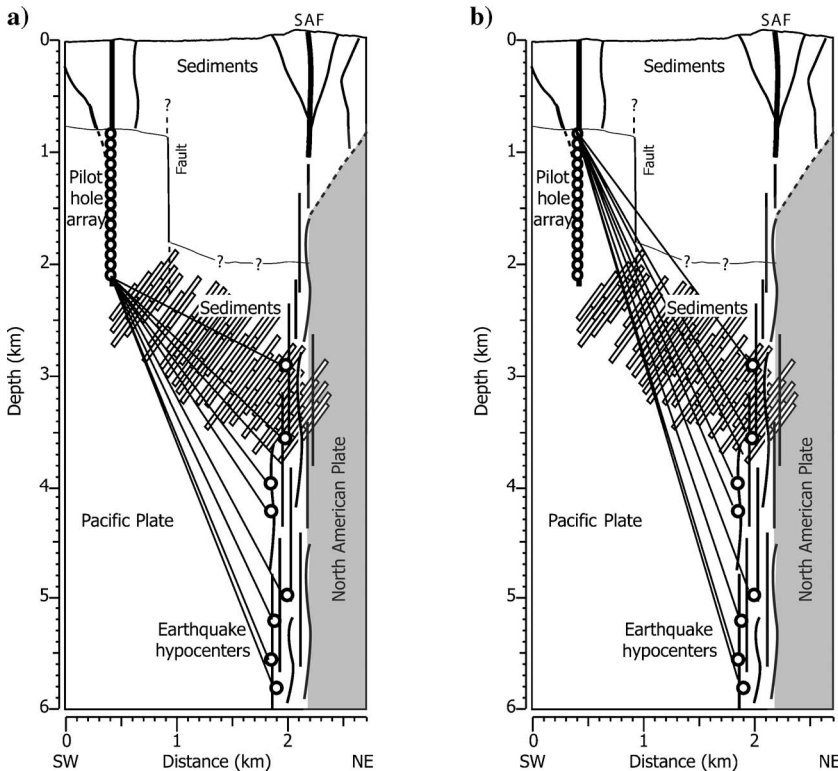

Figure 10. Diagram drawn to scale, showing the pilot-hole array and the nine earthquakes with approximated linear raypaths to (a) lower and (b) upper receivers in the array.

Salinian granite above the sedimentary section, giving rise to the observed stress-induced anisotropy.

DISCUSSION

The separation of stress-induced and structural anisotropy using the formulation in Appendix A allows us to supplement existing stress data in the crust surrounding the SAF in Parkfield, California. Within the sandstone units, where we have modeled stress-induced anisotropy, the fast polarization directions in the sonic logs indicate that $S_{H\max}$ is 0°–45° (north to northeast) within a few hundred meters of the active fault plane. This correlates well with observations of
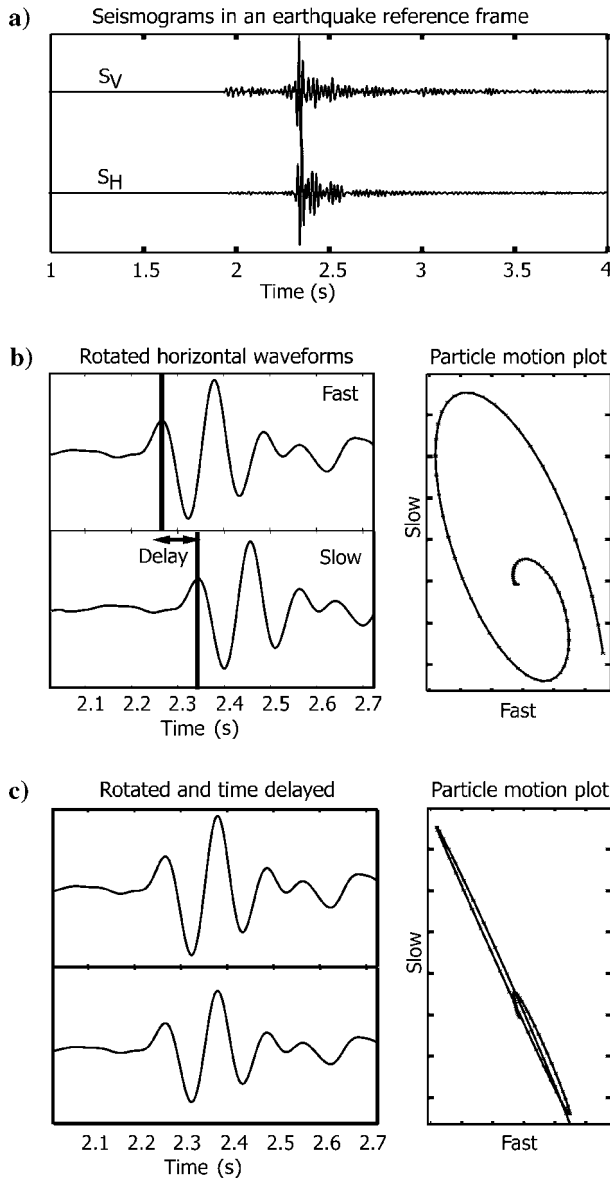
a)

b)

c)

Figure 11. Example of the shear-wave-splitting procedure for one of the nine earthquakes to one of the receivers, showing (a) the original seismograms rotated into an earthquake reference frame, (b) the horizontal waveforms rotated into the fast and slow directions with the corresponding elliptical particle motion plot indicating anisotropy, and (c) the fast and slow seismograms and particle motion plot corrected for anisotropy.

stress from borehole breakouts and tensile cracks in the pilot hole (Hickman and Zoback, 2004), which show a clockwise rotation of $S_{H\max}$ with depth, indicating increasing fault-normal compression deeper in the crust adjacent to the SAF. The results from this analysis support that interpretation, with $S_{H\max}$ estimated to be at an angle of 70° to the strike of the SAF at a vertical depth of 2500 m. We therefore infer the continuation of fault-normal compression to the bottom of the borehole within 200 m lateral distance of the SAF. This implies that the SAF is indeed a weak fault that slips at low levels of resolved shear stress.

Models to explain the weakness of the SAF are abundant in the literature (e.g., Sibson, 1973, 1992; Byerlee, 1990, 1993; Rice, 1992; Sleep and Blanpied, 1992; Brune et al., 1993; Sleep, 1995; Miller, 1996; Melosh, 1996) and include frictionally weak materials in the fault core, high pore pressure that reduces the normal stress, and dynamic weakening mechanisms. However, the significance of many of the models cannot be evaluated because of the uncertainty about the physical properties of the fault zone and the absence of direct measurements of the state of stress, porosity, and permeability. We anticipate that data collected in SAFOD across the fault zone in phase two of drilling will significantly improve our current understanding of the faulting mechanics and strength of the SAF.

Our observations of shear velocity anisotropy at multiple scales illustrate the effect of frequency and scale. Seismic waves are polarized only if the smallest wavelength is much larger than the individual layer thicknesses (Backus, 1962; Berryman, 1979). The dipole sonic logs acquired within SAFOD correspond to wavelengths of investigation on the order of 1.5 m and are subsequently polarized only by the sedimentary bedding in the finely laminated shale when the bedding planes are closely spaced. In contrast, the seismograms recorded on the pilot-hole array from earthquakes approximately 2–4 km away exhibit structural anisotropy for raypaths through the sedimentary sequence, since both the shale and the sandstones have bedding planes at a much closer spacing than the seismic wavelengths of approximately 30 m.
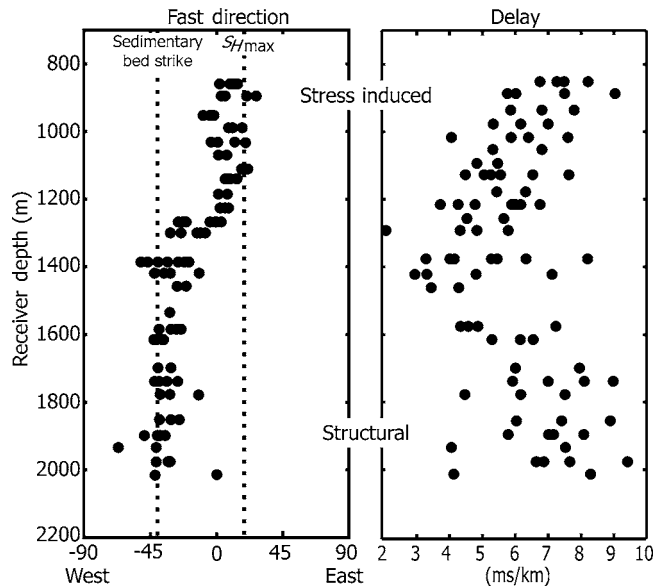

Figure 12. Results from shear-wave-splitting analysis of nine microearthquakes recorded on the pilot-hole array. The strike of the sedimentary bedding planes and the orientation of $S_{H\max}$ are also shown for reference.

The frequency dependence of anisotropy has important implications for the scale length of heterogeneities and in establishing relationships between fractures and permeability anisotropy. Interestingly, the frequency of investigation has a significant effect on the amount of velocity anisotropy. In the sonic log the amount of velocity anisotropy ranges from 2%–10%, whereas at seismic frequencies the amount of anisotropy is 1%–5%. This is in direct contrast to the findings of Liu et al. (2003), who observe a decrease in the amount of velocity anisotropy as the frequency increases for identical shear-wave paths. However, the sonic and seismic waves in this study sample very different volumes of the crust, and the geometry of the raypaths with respect to the formation symmetry axes differ significantly for our sonic and seismic experiments.

Within the sedimentary sequence the lithologic effect on the anisotropy is important at the two different scales. The amount of velocity anisotropy is usually 1%–4% for most rocks below a depth of 1–2 km (Crampin, 1994). However, shales, clays, and mudstones can induce a lithologically controlled anisotropy of several tens of percent. The reason we observe an increase in anisotropy at higher frequencies may be because the sonic waves are traveling over small volumes of highly anisotropic rock associated with the clay-rich sedimentary layers and/or shear zones. The lower amount of anisotropy at seismic frequencies recorded on the pilot hole reflects a loss of resolution because the larger wavelengths average the properties of the anisotropic layers over tens of meters.

In the Parkfield region, the crust is anisotropic as a result of both stress and structure, which act as competing mechanisms. At seismic frequencies, the shear waves are affected by structural anisotropy within the sedimentary sequence, but the polarity of the time delay is reversed because the waves also travel through the granite/sandstones where stress-induced anisotropy is dominant. The integrated time delays from all anisotropic layers along the raypath are much smaller than one would expect if the waves had traveled only through anisotropic layers with the same sense of delay. In contrast, the sonic logs show increased amounts of anisotropy in the sedimentary sequence, but the sonic waves are traveling through a much smaller volume (with homogeneous anisotropy) and thus retain the full anisotropic signature of each lithologic unit.

In addition, the geometry of investigation plays a key role. The seismic raypaths from the earthquakes to the pilot-hole receivers are almost vertical and thus at an oblique angle to the sedimentary bedding, so the horizontal components recorded at the surface are not in a principal direction. In contrast, the sonic logs were acquired in a borehole-formation geometry, so the recorded fast direction is close to the true fast direction of the formation, except in the rare case in which the borehole is exactly perpendicular to the bedding planes and no anisotropy is observed. In other words, the seismic study has lower resolution because of the larger scale of investigation in such a heterogeneous crust, and the geometry of the formation relative to the raypath dictates the maximum anisotropy measured at the receiver.

CONCLUSIONS

We have analyzed shear velocity anisotropy in the crust adjacent to the SAF in Parkfield, California, using dipole sonic shear logs and earthquakes recorded on a vertical 3-C seismic array. In the granite country rock, the fast polarization direction of the shear waves in the vertical section of the pilot hole and main hole is parallel to the direction of the maximum horizontal compressive stress. We suggest this is stress-induced anisotropy caused by the preferential closure of fractures in response to an anisotropic stress state. Our model predicts the fast direction observed for any arbitrary geometry of fast direction resulting from structure and borehole trajectory. For stress-induced anisotropy we show that the apparent fast direction has the same azimuth as the maximum compressive stress, although the dip depends on the orientation of the borehole. In the vertical sections of the pilot hole and main hole, the fast direction observed in the sonic log correlates remarkably well with measurements of S_{Hmax} from borehole breakouts, indicating stress-induced anisotropy. The amount of anisotropy in the granite decreases with depth, as expected for stress-induced anisotropy, because the overall increase of confining pressure with depth closes fractures in all orientations and makes the shear velocity of the rock less sensitive to stress.

In the sedimentary sequence penetrated at depth by SAFOD, the sonic log exhibits two distinct fast shear polarizations: a northeast fast direction in the sandstones and a northwest fast direction in the siltstone and shale units characterized by finely laminated, clay-rich planes. We use our model to show that in the clay-rich shale and siltstone units, the observed fast direction is a result of the sonic shear waves being polarized along the bedding planes. In the well-cemented sandstones (which have physical properties similar to the granite), we observe stress-induced anisotropy. Our theory allows us to examine the importance of the geometry of the borehole relative to both the structural (i.e., bedding) and stress-induced directions of velocity anisotropy when interpreting sonic logs. The observation of a northeast-southwest fast direction is in good agreement with other stress measurements in the region (Townend and Zoback, 2004) and locally at the SAFOD site (Hickman and Zoback, 2004). Our results support the theory of a weak SAF with nearly fault-normal compression at a vertical depth of 2.5 km and at a distance of only several hundred meters to the southwest of the fault.

An analysis of earthquakes recorded on the pilot-hole array at seismic frequencies reveals stress-induced anisotropy at receivers in the top of the array and structural velocity anisotropy for raypaths to receivers in the lower half of the array. We contend this is because raypaths to the upper receivers pass back through the granite, where stress-induced anisotropy dominates and the fast polarization direction observed is highly dependent on the last anisotropic medium encountered.

Structural anisotropy is a stronger mechanism than stress-induced anisotropy at depth, and we observe an increase in delay times at both sonic and seismic frequencies for structural mechanisms. In particular, within clay-rich intervals the intrinsic anisotropy of the clay platelets gives rise to an extremely high anisotropy (up to 10%) at sonic frequencies. This may prove useful as a lithologic indicator. At seismic frequencies the amount of anisotropy is 1%–4% because the longer seismic wavelengths average out the anisotropic effect of many layers. In conclusion, both structural and stress-induced mechanisms control the velocity anisotropy at sonic and seismic frequencies, but our observations have a strong dependence on the scale and geometry of investigation.

ACKNOWLEDGMENTS

APPENDIX A

MODELING SHEAR ANISOTROPY IN AN ARBITRARILY ORIENTED BOREHOLE

The geometry of dipole sonic tools is best suited for investigating transversely isotropic (TI) formations when the borehole is perpendicular to the axis of symmetry (Figure A-1), e.g., parallel to the bedding planes. The shear waves generated and received by the dipole sonic tools are recorded in the planes normal to the axis of the borehole. Thus, the minimum and maximum shear velocities observed (and used to compute the amount of anisotropy) are not necessarily the absolute minimum and maximum velocities in the earth, which may be oriented in directions that are not perpendicular to the borehole axis. We define the true fast direction as the orientation in the earth with the absolute fastest shear velocity (a series of parallel planes described by a dip angle in a specific direction) and the apparent fast direction as the fastest direction in a plane perpendicular to the borehole.

Sinha et al. (1994) model elastic-wave propagation in a borehole with an axis at a range of angles to the formation symmetry axis. They demonstrate how the amount of anisotropy varies as the borehole becomes more oblique to the symmetry axis of the formation and that the maximum anisotropy is recorded at a 90° angle. The geometry of the borehole relative to the formation will not only dictate the amount of anisotropy observed but also the apparent fast direction recorded by the tool. Figure A-1 illustrates the case when the borehole (and thus shear-wave propagation) is either parallel or perpendicular to the TI axis of symmetry. However, in reality the borehole probably will be at some oblique angle to the symmetry axis (Figure A-1a), and more generally neither the borehole nor the formation will align with the vertical or horizontal coordinate axes (Figure A-1b).

We present a 3D model for computing the apparent fast direction to be recorded on the dipole sonic tools for any arbitrary orientation of the borehole and formation. Figure A-2 shows the geometry used in our model. In the case of stress-induced anisotropy, the true fast direction is parallel to the maximum compressive stress, oriented across the closed fractures. Unless the borehole is oriented exactly along the TI symmetry axis, the apparent fast direction is described by a unique line that lies within the plane normal to the borehole, in the direction normal to the fracture opening direction. Since SAFOD is in a strike-slip/reverse stress state, we expect the maximum compressive stress to be horizontal; thus, the fastest shear velocity will be described by an azimuth in the horizontal plane.

The apparent fast direction is the vertical projection of the maximum compressive stress on the plane perpendicular to the borehole and has the same azimuth as S_{Hmax} (Figure A-2b), with a dip that depends on borehole orientation. In the case of structural anisotropy, the true fast direction is oriented along the planes (be they fractures/bedding/aligned minerals), and the orientation is dependent on the propagation direction. However, the apparent fast direction must be in the plane perpendicular to the borehole. Therefore, the apparent fast direction observed with the sonic tool is an azimuth that lies in both the true fast plane and the plane normal to the borehole, i.e., a line that marks the intersection of both planes (Figure A-2c). Our formalism allows one either to determine the true fast direction in the earth given an observed apparent fast direction or, if the formation geometry is known, to predict the apparent fast direction recorded by the dipole sonic tool for the assumed TI formation.
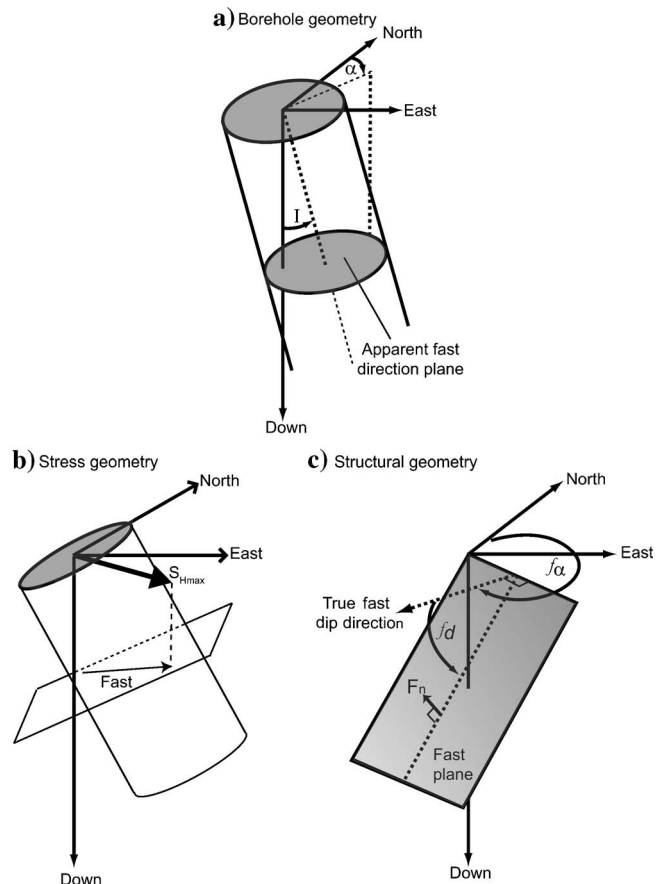
Figure A-2. (a) The geometry of the borehole with the plane in which the apparent fast direction is measured with the sonic logs. (b) In the case of stress-induced anisotropy, the apparent fast direction in the plane perpendicular to the borehole has an azimuth equivalent to that of S_{Hmax}, although the dip depends on the borehole trajectory. (c) Geometry used to compute the apparent fast direction that will be observed on the dipole sonic tool for structural anisotropy when the fast direction lies in an arbitrarily oriented plane.
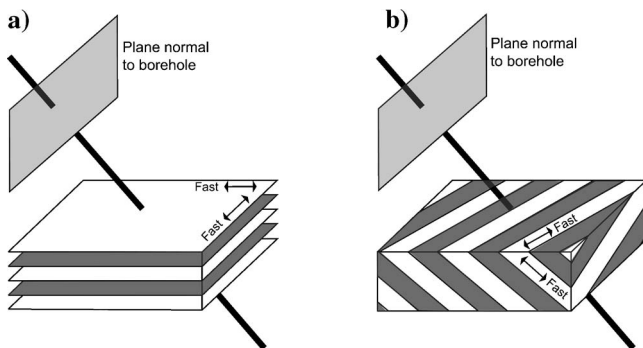

Figure A-1. (a) Geometry of a borehole at an oblique angle to a vertically transverse formation. (b) The general case when a borehole is oblique to a formation with a symmetry axis that is not aligned with one of the Cartesian coordinate axes.
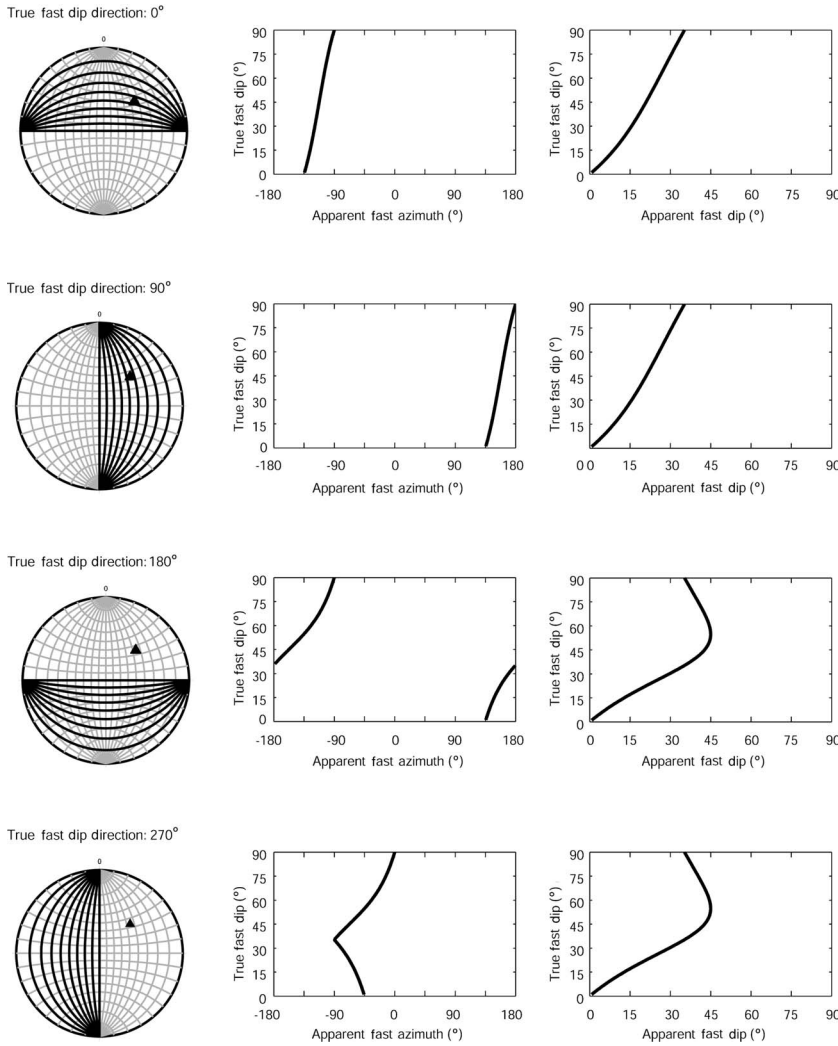
Figure A-3. Model results for the arbitrary case of a borehole with an azimuth of 45° inclined at 45° (shown as a triangle on the stereonets) for four true fast dip directions of 0°, 90°, 180°, and 270° at a full range of dips from 0°–90° (shown as great circles).

describes the apparent fast direction f^a_d (defined to be in the dip direction) and the apparent fast dip f^a_α from the origin are then found by computing the line perpendicular to the borehole and to the normal to the fast plane (i.e., in the fast plane) such that $\mathbf{f^a} = \mathbf{b_n} \times \mathbf{f_n}$.

Figure A-3 shows the results of this computation for the arbitrary case of a well with an azimuth of 45° (i.e., northeast) and an inclination of 45°. We show the apparent fast direction and dip that will be measured in the borehole for true fast directions dipping to the north, east, south, and west (i.e., 0°, 90°, 180°, and 270°) over a range of true fast dip angles from horizontal to vertical (i.e., 0°–90°). Typically the azimuth of the fast direction is reported (as a direction between −90° west and 90° east), but the dip of the fast direction is omitted because only vertical TI symmetry is considered. However, given the orientation of the borehole, the dip of the apparent fast direction can be computed easily because the observed azimuth lies in a plane normal to the borehole. For completeness we present both the azimuth (as an angle between 180° and 180° in the direction of dip) and the dip of the apparent fast direction. We also show that the dip of the fast azimuth provides valuable information about the true orientation of the fast direction within the formation.

Figure A-3 illustrates the strong dependence that the relative geometry of the borehole and true fast direction (shown here as a bedding plane) have on the apparent fast direction. In this example with a northeast-trending borehole, one can see that if the beds dip to the north, the apparent fast direction will be southwest. However, if the beds dip to the east, the apparent fast direction is southeast. When the bedding planes are either close to horizontal or vertical, the true fast direction is hard to determine from the apparent fast direction. Otherwise, the results from this modeling indicate that the true fast directions will give rise to a unique apparent fast direction in the borehole.

For this borehole trajectory, the dip of the true fast direction (or bedding planes) has the biggest effect on the apparent fast direction when the beds are dipping to the south and west, i.e., away from the direction of penetration. The true fast direction is most closely approximated by the apparent fast direction when the formation axis is close to being perpendicular to the borehole. This corresponds to the results of Sinha et al. (1994), showing the amount of anisotropy will also be at a maximum when the formation axis is normal to the borehole.

As shown in Figure A-2a, for a borehole with azimuth from north α and inclination from the vertical I, the vector $\mathbf{b_n}$, which defines the axis of the borehole from an arbitrary origin, is given by

$$\mathbf{b}_n = \left[\sin(\alpha) \sqrt{1 + \left(\sin\left(\frac{\pi}{2} - I\right) \right)^2} \right.$$
$$\left. \times \cos(\alpha) \sqrt{1 + \left(\sin\left(\frac{\pi}{2} - I\right) \right)^2} - \sin\left(\frac{\pi}{2} - I\right) \right],$$
(A-1)

where all angles are in radians. Given the dip f_d and dip direction f_α of the true fast plane, we compute three discrete points $\mathbf{f_1}, \mathbf{f_2}$, and $\mathbf{f_3}$ in the fast plane that has a corner at the origin used to define the borehole. The normal to the fast plane, $\mathbf{f}_n$, may now be computed using $\mathbf{a} = \mathbf{f_1} - \mathbf{f_2}$ and $\mathbf{b} = \mathbf{f_2} - \mathbf{f_3}$, thus giving $\mathbf{f}_n = a \times b$. The vector $\mathbf{f^a}$ that

REFERENCES

Alford, R. M., 1986, Shear data in the presence of azimuthal anisotropy: 56th Annual International Meeting, SEG, Expanded Abstracts, 476–479.
Almeida, R., J. Chester, T. J. Waller, and D. Kirschner, 2005, Lithology and structure of SAFOD Phase I core samples: EOS, Transactions of the American Geophysical Union, **86**, T21A–0454
Anderberg, M. R., 1973, Cluster analysis for applications: Academic Press, Inc.

Backus, M., 1962, Long-wave elastic anisotropy produced by horizontal layering: Journal of Geophysical Research, **67**, 4427–4440.

Bakun, W. H., and T. V. McEvilly, 1984, Recurrence models and Parkfield, California earthquakes: Journal of Geophysical Research, **89**, 3051–3058.

Barton, C. A., and M. D. Zoback, 1994, Stress perturbations associated with active faults penetrated by boreholes: Possible evidence for near-complete stress drop and a new technique for stress magnitude measurement: Journal of Geophysical Research, **99**, 9373–9390.

Berryman, J. G., 1979, Long-wave elastic anisotropy in transversely isotropic media: Geophysics, **44**, 897–917.

Boness, N. L., and M. D. Zoback, 2004, Stress-induced seismic velocity anisotropy and physical properties in the SAFOD pilot hole in Parkfield, CA: Geophysical Research Letters, **31**, L15S17.

Booth, D. C., and S. Crampin, 1985, Shear-wave polarizations on a curved wavefront at an isotropic free-surface: Geophysical Journal of the Royal Astronomical Society, **83**, 31–45.

Brune, J. N., T. L. Henyey, and R. F. Roy, 1969, Heat flow, stress, and rate of slip along the San Andreas fault, California: Journal of Geophysical Research, **74**, 3821–3827.

Brune, J. N., S. Brown, and P. A. Johnson, 1993, Rupture mechanism and interface separation in foam rubber models of earthquakes: A possible solution to the heat flow paradox and the paradox of large overthrusts: Tectonophysics, **218**, 59–67.

Byerlee, J., 1990, Friction, overpressure and fault normal compression: Geophysical Research Letters, **17**, 2109–2112.

——, 1993, Model for episodic flow of high-pressure water in fault zones before earthquakes: Geology, **21**, 303–306.

Chavarria, J. A., P. E. Malin, and E. Shalev, 2004, The SAFOD pilot hole seismic array: Wave propagation effects as a function of sensor depth and source location: Geophysical Research Letters, **31**, L12S07.

Chen, S. T., 1988, Shear-wave logging with dipole sources: Geophysics, **53**, 659–667.

Crampin, S., 1986, Anisotropy and transverse isotropy: Geophysical Prospecting, **34**, 94–99.

——, 1991, Wave propagation through fluid-filled inclusions of various shapes: Interpretation of extensive dilatancy anisotropy: Geophysical Journal International, **107**, 611–623.

——, 1994, The fracture criticality of crustal rocks: Geophysical Journal International, **118**, 428–438.

Crampin, S., and J. H. Lovell, 1991, A decade of shear-wave splitting in the earth's crust, What does it mean? What use can we make of it? And what should we do next?: Geophysical Journal International, **107**, 387–419.

Darot, M., and J. L. Bouchez, 1976, Study of directional data distributions from principal preferred orientation axes: Journal of Geology, 84, 239–247.

Esmersoy, C., K. Koster, M. Williams, A. Boyd, and M. Kane, 1994, Dipole shear anisotropy logging: 64th Annual International Meeting, SEG, Expanded Abstracts, 1139–1142.

Fisher, N. I., T. Lewis, and B. J. J. Embleton, 1987, Statistical analysis of spherical data: Cambridge University Press.

Harrison, A. R., C. J. Randall, J. B. Aron, C. F. Morris, A. H. Wignall, and R. A. Dworak, 1990, Acquisition and analysis of sonic waveforms from a borehole monopole and dipole source for the determination of compressional and shear speeds and their relation to rock mechanical properties and surface seismic data: Annual Technical Conference and Exhibition, Society of Petroleum Engineers, Paper 20557.

Hickman, S., and M. D. Zoback, 2004, Stress orientations and magnitudes in the SAFOD pilot hole from observations of borehole failure: Geophysical Research Letters, **31**, L15S12.

Hickson, T. A., 1999, A study of deep-water deposition: Constraints on the sedimentation mechanics of slurry flows and high-concentration turbidity currents, and the facies architecture of a conglomeratic channel-overbank system: Ph.D. dissertation, Stanford University.

Hickson, T. A., and D. R. Lowe, 2002, Facies architecture of a submarine fan channel-levee complex: Juniper Ridge conglomerate, Coalinga, California: Sedimentology, **49**, 335–362.

Hornby, B. E., 1998, Experimental laboratory determination of the dynamic elastic properties of wet, drained shales: Journal of Geophysical Research, **103**, 29945–29964.

Jaeger, J., and N. G. W. Cook, 1979, Fundamentals of rock mechanics, 3rd ed.: Chapman & Hall.

Johnston, J. E., and N. I. Christensen, 1995, Seismic anisotropy of shales: Journal of Geophysical Research, **100**, 5991–6003.

Jurkevics, A., 1988, Polarization analysis of three-component array data: Bulletin of the Seismological Society of America, **78**, 1725–1743.

Kimball, C. V., and T. M. Marzetta, 1984, Semblance processing of borehole acoustic array data: Geophysics, **49**, 264–281.

Kiraly, L., 1969, Statistical analysis (orientation and density): Geologische Rundshau, **59**, 125–151.

Lachenbruch, A. H., and J. H. Sass, 1980, Heat flow and energetics of the San Andreas fault zone: Journal of Geophysical Research, **85**, 6185–6223.

Leslie, H. D., and C. J. Randall, 1990, Eccentric dipole sources in fluid-filled boreholes: Experimental and numerical results: Journal of the Acoustical Society of America, **87**, 2405–2421.

Liu, E., S. Crampin, J. H. Queen, and W. D. Rizer, 1993, Behavior of shear waves in rocks with two sets of parallel cracks: Geophysical Journal International, **113**, 509–517.

Liu, E., J. H. Queen, X.-Y. Li, M. Chapman, H. B. Lynn, and E. M. Chesnokov, 2003, Analysis of frequency-dependent seismic anisotropy from a multicomponent VSP at Bluebell-Altamont field, Utah: Journal of Applied Geophysics, **54**, 319–333.

Lowe, D. R., 1972, Implications of three submarine mass-movement deposits, Cretaceous, Sacramento Valley, California: Journal of Sedimentary Petrology, **42**, 89–101.

Lynn, H. B., and L. A. Thomsen, 1986, Shear-wave exploration along the principal axes: 56th Annual International Meeting, SEG, Expanded Abstracts, 473–476.

Meadows, M., and D. Winterstein, 1994, Seismic detection of a hydraulic fracture from shear-wave VSP data at Lost Hills field, California: Geophysics, **57**, 11–26.

Melosh, H. J., 1996, Dynamical weakening of faults by acoustic fluidization: Nature, **379**, 601–606.

Miller, S. A., 1996, Fluid-mediated influence of adjacent thrusting on seismic cycle at Parkfield: Nature, **382**, 799–802.

Moos, D., and M. D. Zoback, 1983, In-situ studies of velocity in fractured crystalline rocks: Journal of Geophysical Research, **88**, 2345–2358.

Mount, V. S., and J. Suppe, 1987, State of stress near the San Andreas fault: Implications for wrench tectonics: Geology, **15**, 1143–1146.

Mueller, M. C., 1991, Prediction of lateral variability in fracture intensity using multicomponent shear-wave seismic as a precursor to horizontal drilling: Geophysical Journal International, **107**, 409–415.

——, 1992, Using shear waves to predict lateral variability in vertical fracture intensity: The Leading Edge, **33**, 29–35.

Nur, A., and G. Simmons, 1969, Stress induced velocity anisotropy in rock: An experimental study: Journal of Geophysical Research, **74**, 6667–6674.

Nuttli, O., 1961, The effect of the earth's surface on the S wave particle motion: Bulletin of the Seismological Society of America, **44**, 237–246.

Rice, J. R., 1992, Fault stress states, pore pressure distributions, and the weakness of the San Andreas fault, *in* B. Evans and T. Wong, eds., Fault mechanics and transport properties of rocks: Academic Press, Inc., 475–503.

Roeloffs, E., and J. Langbein, 1994, The earthquake prediction experiment at Parkfield, California: Reviews of Geophysics, **32**, 315–336.

Sayers, C. M., 1994, The elastic anisotropy of shales: Journal of Geophysical Research, **99**, 767–774.

Schlumberger, 1995, DSI* Dipole Shear Sonic Image: Oilfield Marketing Services, Schlumberger.

Shamir, G., and M. D. Zoback, 1992, Stress orientation profile to 3.5 km depth near the San Andreas fault at Cajon Pass, California: Journal of Geophysical Research, **97**, 5059–5080.

Sibson, R. H., 1973, Interactions between temperature and pore-fluid pressure during earthquake faulting and a mechanism for partial or total stress relief: Nature, **243**, 66–68.

——, 1992, Implications of fault-valve behavior for rupture nucleation and recurrence: Tectonophysics, **211**, 283–293.

Silver, P. G., and W. W. Chan, 1991, Shear wave splitting and subcontinental mantle deformation: Journal of Geophysical Research, **96**, 16429–16454.

Sinha, B. K., and S. Kostek, 1996, Stress-induced azimuthal anisotropy in borehole flexural waves: Geophysics, **61**, 1899–1907.

Sinha, B. K., A. N. Norris, and S.-K. Chang, 1994, Borehole flexural modes in anisotropic formations: Geophysics, **59**, 1037–1052.

Sleep, N. H., 1995, Ductile creep, compaction, and rate and state dependent friction within major fault zones: Journal of Geophysical Research, **100**, 13065–13080.

Sleep, N. H., and M. L. Blanpied, 1992, Creep, compaction and the weak rheology of major faults: Nature, **359**, 687–692.

Thomsen, L., 1986, Weak elastic anisotropy: Geophysics, **51**, 1954–1966.

Townend, J., and M. D. Zoback, 2001, Implications of earthquake focal mechanisms for the frictional strength of the San Andreas fault system, *in* R. E. Holdsworth, R. A. Strachan, J. F. Magloughlin, and R. J. Knipe, eds, The nature and significance of fault zone weakening: Geological Society of London Special Publication, 186, 13–21.

——, 2004, Regional tectonic stress near the San Andreas fault in central and southern California: Geophysical Research Letters, **31**, L15S11.

Williams, C. F., F. V. Grubb, and S. P. Galanis, Jr., 2004, Heat flow in the SAFOD pilot hole and implications for the strength of the San Andreas fault: Geophysical Research Letters, **31**, L15S14.

Willis, H., G. Rethford, and E. Bielanski, 1986, Azimuthal anisotropy, Occurrence and effect on shear wave data quality: 56th Annual International Meeting, SEG, Expanded Abstracts, 479–481.

Winkler, K. W., B. K. Sinha, and T. J. Plona, 1998, Effects of borehole stress concentrations on dipole anisotropy measurements: Geophysics, **63**, 11–17.

Zhang, Z., and S. Y. Schwartz, 1994, Seismic anisotropy in the shallow crust of the Loma Prieta segment of the San Andreas fault system: Journal of Geophysical Research, **99**, 9651–9661.

Zinke, J. C., and M. D. Zoback, 2000, Structure-related and stress-induced shear wave velocity anisotropy: Observations from microearthquakes near the Calaveras fault in central California: Bulletin of the Seismological Society of America, **90**, 1305–1312.

Zoback, M. D., M. L. Zoback, V. S. Mount, J. Suppe, J. P. Eaton, J. H. Healy, D. Oppenheimer, P. Reasenberg, L. Jones, C. B. Raleigh et al., 1987, New evidence on the state of stress of the San Andreas fault system: Science, **238**, 1105–1111.